Journal of the Meteorological Society of Japan

EARLY ONLINE RELEASE

The DOI for this manuscript is
DOI:10.2151/jmsj.2022-040
J-STAGE Advance published date: June 6th, 2022
The final manuscript after publication will replace the preliminary version at the above DOI once it is available.

Possible roles of the sea surface temperature warming of the Pacific Meridional Mode and the Indian Ocean warming on tropical cyclone genesis over the North Pacific for the super El Niño in 2015

Takahiro ISHIYAMA

Atmosphere and Ocean Research Institute
The University of Tokyo, Kashiwa, Japan

Masaki SATOH

Atmosphere and Ocean Research Institute
The University of Tokyo, Chiba, Japan

Yohei YAMADA

Japan Agency for Marine-Earth Science and Technology, Yokohama, Japan

Revised May 25, 2022

----

1) Corresponding author: Masaki Satoh, Atmosphere and Ocean Research Institute University of Tokyo, 5-1-5, Kashiwanoha, Kashiwa-shi, Chiba 277-8564 JAPAN.
Email: satoh@aori.u-tokyo.ac.jp
Tel: +81-4-7136-6050
Fax: +81-4-7136-6056

Abstract

This study reveals the potential roles of the sea surface temperature (SST) warming associated with the Pacific Meridional Mode (PMM) and the Indian Ocean (IO) warming on tropical cyclone genesis (TCG) in the North Pacific (NP) by focusing on the super El Niño event that occurred in 2015. We used the global non-hydrostatic model to conduct perpetual experiments by integrating for 30 months to obtain a climatological condition of July 2015 and examine sensitivities to SST in the warming region of PMM and IO on TCG over NP. We showed that if SST associated with PMM is warmer, the monsoon trough in the western North Pacific (WNP) and vertical wind shear over the eastern North Pacific (ENP) become weaker, causing reduced TCG in WNP and increased TCG in ENP. We also showed that if SST over IO is warmer, the monsoon trough in WNP becomes weaker, although the vertical wind shear over ENP does not appreciably change. We found that with SST warming associated with PMM or over IO, the anticyclonic anomalies over WNP intensify. We confirmed that if SST is warmer for PMM in the absence of the El Niño forcing, the cyclonic anomalies over WNP

intensify as in previous studies. The present results imply a non-linear response for the forcing of the warm SST associated with PMM and El Niño.

Keywords: tropical cyclone; El Niño; Pacific Meridional Mode; monsoon trough; vertical shear

1. Introduction

The year 2015 was reported to have experienced the largest El Niño event, while the second-largest event occurred in 1997, based on the records from 1950 to 2017 (L'Heureux et al. 2017; Timmermann et al. 2018). During the latter El Niño event, tropical cyclone (hereafter TC) activity over the North Pacific (hereafter NP) was particularly enhanced. Bluden et al. (2016) showed that in 2015, accumulated cyclone energy was 479×10^4 kt^2 over the Western North Pacific (hereafter WNP) and 288×10^4 kt^2 over the Eastern North Pacific (hereafter ENP), both higher than their respective climatological median values (305 for WPN and 119 for EPN). The number of intense TCs was 16 over WNP and 11 over ENP, which were also higher than the climatological median values of 9 and 4, respectively. In addition, the number of named TCs was 26 over the ENP (higher than the climatological median of 17), while the number of TCs over WNP was approximately the same as the climatological median.

In general, El Niño modulates TC activity over WNP. During the super El Niño years, the frequency of intense TCs increases and the lifetime of TCs becomes longer, and the average position of TC genesis (hereafter TCG) shifts more southeastward (Chan 2000; Wang and Chan 2002; Chan and Liu 2004; Camargo and Sobel 2005; Chen et al. 2006). When super El Niño occurs, the monsoon trough, characterized by westerly wind over WNP near the equator, extends eastward, leading to an active TC genesis over WNP (Lander 1994; Wu et al. 2012). In addition, over ENP, the intensity, frequency, and lifetime of the TCs generally increase, and the average position of TCGs shifts westwards (Irwin and Davis 1999; Chu 2004; Camargo et al. 2008; Kim et al. 2011; Jin et al. 2014; Fu et al. 2017).

In 2015, in addition to the super El Niño event, the sea surface temperature (SST) was also warmer over the Indian Ocean (hereafter IO) and the region of the Pacific Meridional Mode (hereafter PMM; Chiang and Vimont 2004) as shown by Fig. 1a. When IO is warmer, it is well known that over WNP, the anticyclones become stronger (Xie et al. 2009), and TCG is suppressed (Zhan et al. 2011; Ha et al. 2015).

During the positive phase of PMM (hereafter PPMM), TCG over both WNP and ENP is enhanced owing to the cyclonic anomaly over WNP and weaker vertical wind shear over ENP (Zhang et al. 2016; Murakami et al. 2017; Gao et al. 2018).

Previous studies have examined the dependence of TCG over NP on super El Niño events, IO warming, and PMM. However, the relative roles of the forcings in the three regions (the warm SST regions associated with El Niño and PMM, IO) are not yet clearly understood thus far. Therefore, we focus on the 2015 El Niño event and investigate the influence of the IO warming and PPMM on TCG over NP.

To examine the relative roles of SST anomalies (hereafter SSTAs), we conducted perpetual sensitivity experiments (Cess and Potter 1988; Iga et al. 2007) by changing the SST patterns associated with PMM and the IO warming using the Non-hydrostatic Icosahedral Atmospheric Model (hereafter NICAM; Tomita and Satoh 2004; Satoh et al. 2008, 2014).

This paper is organized as follows: First, in Section 2, the model used in this study is described, together with the experimental settings, method of TC detection, and SST settings. The result of the control experiment taking the climatological conditions of July 2015 is presented in Section 3. Results of the sensitivity experiments are presented in Section 4, discussed in Section 5, and summarized in Section 6.

2. Experimental settings and the TC detection method

2.1 Model setting

We use NICAM with a horizontal resolution of 56 km for conducting perpetual experiments to determine the sensitivity of TC activity to SST patterns. Grid resolution of 56 km is chosen to reduce computational requirements. NICAM is generally used at a 14 km or finer horizontal resolution. This model also reproduces the multi-scale structure of convection systems with realistic atmospheric circulation (Kodama et al. 2015; Satoh et al. 2017). NICAM with a horizontal resolution of 14 km or less has been used to study the Madden–Julian oscillation and TCs (e.g., Miura et al. 2007; Miyakawa et al. 2014; Nakano et al. 2015; Satoh et al. 2015; Yamada et al. 2017, 2019, 2021). It has also been shown that NICAM at coarser resolutions (e.g., 56–220 km) can realistically reproduce the behaviors of convection systems (e.g., their intra-seasonal variability in the tropics) without cumulus parameterization (Yoshizaki et al. 2012; Takasuka et al. 2015, 2018; Kodama et al. 2021; Chikira et al. 2022). Based on these studies, numerical experiments in this study were conducted using the 56 km horizontal resolution grid without cumulus parameterization. For the cloud microphysics scheme, we use the NICAM single-moment water six-cloud microphysics scheme (NSW6; Tomita 2008); for the planetary boundary layer (PBL) scheme, we use the Mellor Yamada Nakanishi Niino Planetary boundary layer (MYNN scheme; Nakanishi and Niino 2004); for the radiative transfer process mstrnX is used (Sekiguchi and Nakajima 2008); and the minimal advanced treatments of surface interaction and runoff (MATSIRO; Takata et al. 2003) is used for the land surface model.

2.2 Perpetual experiment

A perpetual experiment is an experiment that is conducted without seasonal change. The SST distribution of the control experiment (CTL) and the solar radiation were fixed for the climatological conditions of July; the conditions were defined by the monthly mean of the control SST and solar radiation. Diurnal variations exist for solar radiation. To obtain the initial field of the atmospheric conditions, we used the Japanese 55-year Reanalysis (hereafter JRA-55; Kobayashi et al. 2015). Simulations were integrated from 00:00 UTC on July 1, 2015. In addition, we used the initial value of land pre-adjusted with low-resolution NICAM (Kodama et al. 2015). For SST, the NOAA Optimum Interpolation SST V2 dataset was used. Figure 1 shows the SST patterns [30°E–85°W, 60°S–60°N] used in the experiments (CTL; Fig. 1a) and sensitivity experiments (Figs. 1b-g); the contours represent the values of SST, and the colors show the deviation from the climatological values defined as the July average for the period 1982-2011.

We defined three oceanic regions; the warm SST region related to El Niño [160°E–80°W, 10°S–10°N] (hereafter referred to as the El Niño region), the warm SST region related to PMM [10–45°N, 110–180°W] (hereafter referred to as the PMM region) and the IO region [5–30°S, 30–140°E] and [5°S–30°N, 30–100°E]. We define the PMM region just north of the El Niiño region as a warm SST region associated with PMM. This definition is different from that used by Chiang and Vimont (2004). In the previous studies on TCG, the effects of SST warming over specific regions are considered (Murakami et al. 2017). We follow their approach and consider the effect of SST warming over the PMM and El Niiño regions and the IO warming.

We conducted six sensitivity experiments to examine the SST perturbations in these regions. The first experiment is the "Allclm" experiment (Fig. 1b), wherein climatological SST is used in all regions. The second (Fig. 1c) and the third (Fig. 1d) experiments are sensitivities to CTL (Fig. 1a); Fig. 1c replaced the SSTA over the PMM region in 2015 by climatological SST (referred to as "PMMclm" experiment), and Fig. 1d replaces SSTA over the IO in 2015 by climatological SST (referred to as "IOclm" experiment). The remaining three experiments are for sensitivities to the "Allclm" experiment (Fig. 1b). Fig. 1e is the " PMM/El Niño2015" experiment, in which we added SSTAs over the PMM and El Niño regions; Fig. 1f is the "El Niño2015" experiment where SSTA of July 2015 is added to the El Niño region; Fig. 1g is the "PMM2015" experiment where SSTA of July 2015 is added to the PMM region. Table 1 provides a clear overview of the changes in the SST for the study regions in these sensitivity experiments.

The simulation was conducted for 46 months; the results of months 16–46 were used for analysis, while the first 15 months were discarded as the spin-up period. For the perpetual experiments representing 30 months, we regarded the results of TCG for each month as one sample and statistically analyzed the TCG results of all 30 samples.

Because the experiment is under the perpetual condition, the land surface temperature is generally warmer than that recorded in the observations. Figure 2 shows the time series of land surface temperature over the selected two domains; eastern Eurasia [60–120°E, 50–60°N] (black curve) and the Indo-Chinese Peninsula [98–106°E, 14–24°N] (blue curve). Eastern Eurasia shows a relatively larger change in surface temperature. Figure 2 shows a continuous increase in temperature from the initial month to approximately the 15th month, after which it fluctuates about the quasi-equilibrium state. The land surface temperature bias is larger at higher latitudes and moderates in the tropical and sub-tropical regions.

However, the surface temperature near the Indo-Chinese Peninsula shows quasi-equilibrium from the initial month.

In this paper, we show the distribution of TCG in each experiment by analyzing the 30-month data; similarly, the zonal fields of the atmosphere are also averaged for 30 months.

2.3 Detection method

The TC detection method is based on those suggested by Oouchi et al. (2006), Nakano et al. (2015), and Yamada et al. (2017); a TC is identified, provided the following criteria are satisfied for the duration of at least 36 h: (i) the 10 m wind speed is greater than 17.5 m s^{-1}, (ii) the sum of a temperature anomaly at 700 hPa, 500 hPa, and 300 hPa is greater than 2 K in a warm core, and (iii) the relative vorticity at 850hPa is greater than 3.5×10^{-5} s^{-1}. According to Walsh et al. (2007), a wind speed of 17.5 m s^{-1} is a suitable threshold for TC detection for the present 56-km grid model results.

2.4 Observed data and reanalysis data

To compare the result of CTL with the observed data, we used the International Best Track Archive for Climate Stewardship (IBTrACS; Knapp et al. 2010) for TC activity and JRA-55 monthly data for atmosphere. As the perpetual experiment represents a statistical equilibrium over the summer season, we used the data averaged for July, August, and September (hereafter JAS).

2.5 Vertical shear

The vertical shear is calculated using the following equation:

$$\text{Vertical Wind Shear} = \sqrt{(u_{200hPa} - u_{850hPa})^2 + (v_{200hPa} - v_{850hPa})^2} \qquad (1)$$

where u_{200hPa} and u_{850hPa} are the zonal winds at 200hPa and 850hPa (m s^{-1}), respectively, and v_{200hPa} and v_{850hPa} are the meridional winds at 200hPa and 850hPa (m s^{-1}), respectively.

3. Results

3.1 Comparison of the atmospheric circulation

The results of our experiments well reproduce the characteristics of the atmospheric field in July 2015. Figure 3 shows the patterns of sea level pressure (hereafter SLP) and 850hPa zonal winds of CTL by Figs. 3a and 3c, respectively, and those of JRA-55 are shown by Figs. 3b and 3d.

Figures 3a and 3b show that the strength of the Pacific high of CTL is stronger than that of JRA-55, possibly due to the setting of the perpetual July experiment. Figure 2 shows that the surface temperature over the Eurasian Continent of CTL is significantly warmer than the initial condition. Moreover, the contrast in surface temperature between the Eurasian Continent and the Pacific Ocean is larger in simulations than in observations. This contrast can be reduced if the simulated land surface temperature is closer to the observed field.

However, the differences in the climate values of both data sets show a positive anomaly over the region from IO to the western part of WNP and a negative anomaly from ENP to the region around Japan. These results indicate that CTL shows the bias of high-pressure anomaly. Still, the difference between

CTL and the Allclm experiment (Fig. 3c) is similar to JRA-55 between the climatology and July 2015 (Fig. 3d).

Figures 3c and 3d show that in CTL, the easterlies along 20°N in NP are generally stronger than for JRA-55, while the westerlies over WNP are weaker. However, the region of the westerlies near the equatorial western Pacific, i.e., the monsoon trough, is reproduced in a similar region, from the maritime continent to the dateline. The activity of the monsoon trough is closely related to that of the tropical cyclones in WNP, as previously reported (Lander 1994; Wu et al. 2012; Yamada et al. 2019).

CTL can reproduce the atmospheric circulation only to a certain extent, compared to the 2015 observations or the difference from the climatology. Despite these drawbacks, TC activity in the Pacific shows similarities between the experimental and observed values. Thus, we regard that this experiment is usable as CTL.

3.2 TC activity and environmental fields

Figure 4 shows the geographic distribution of TCG in CTL. The number of TCs is larger in the experiment than in the observations because the experimental duration is 30 times longer than the observational duration (July 2015; one month). The positions of TCG in the experiment are similar to those in the observation, although the quantitative comparison is not applicable.

Figure 5 shows the boxplot of the number of TCs in each region for CTL. The red circles in Fig. 5 are the observed number of TCG points in July 2015. The observed genesis numbers over NP, WNP and ENP are 8, 3, and 5, respectively, and these are within the simulated probability range presented by the boxes. Specifically, over NP and WNP, the observed genesis numbers are within the 25^{th} to 75^{th} percentile of all samples. The observed genesis number for ENP is within the top 25 percentiles of all the samples.

It should be noted that the observed value need not be close to the median of the sample of the simulation values, even if the model's bias is small. Yamada et al. (2019) conducted 50-member ensemble simulations for the summer seasons of multiple years, including 2015, and showed that the TC number of the ensemble mean of 2015 deviated from the observed value. It is also possible that the relatively coarse horizontal resolution in this simulation might have led to less frequent TCG over ENP. The horizontal scale of TCs over the ENP is generally smaller than that over other basins (Knaff et al. 2007; Chavas and Emanuel 2010), so a higher resolution is required to reproduce TCG over ENP realistically. The simulation of TCG over ENP is difficult, as indicated by most models participated in Coupled Model Intercomparison Project Phase 5 and 6 (CMIP5 and CMIP6, respectively) (Camargo 2013; Roberts et al. 2020).

We also examined the environmental fields of TCG. Among the components related to TCG, we focus on the vertical wind shear and the zonal wind at 850hPa. The strength of the zonal wind at 850hPa in the equatorial region of the western Pacific indicates the activity of the monsoon trough. It is related to vorticity, which comprises the Genesis Potential Index (Emanuel and Nolan 2004). It is known that the activity of the monsoon trough is related to TCG in WNP (Wu et al. 2012).

Figure 6 shows the relationship between the temporal variability of the monsoon trough and TCG over the WNP by the time–longitude Hovmöller diagrams. It presents the diagram of zonal winds averaged in the latitudinal belt between 0°N and 5°N (located to the south of the active TCG region over WNP). Figure 6 shows that the westerly winds in the experiment frequently extend eastwards and occasionally progress further east beyond the dateline; this occurs when relatively stronger TCs are generated (Chen et al. 2006; Yamada et al. 2019).

Figure 6 also shows that when westerly winds extend eastwards, TCG often occurs over WNP. This result indicates that TCG and the fluctuation of the westerly winds correspond well; for example, TCG often occurs within the monsoon shear line. Previous studies have reported similar results (Ritchie and Holland 1997; Yoshida and Ishikawa 2013). The fluctuation in the westerlies also explains variations in the number of TCG over WNP (Fig. 5). If the westerlies are stronger, TCG is more frequent, whereas if the westerlies are weaker, TCG becomes occasional.

Figure 7 shows the vertical wind shear of CTL and JRA-55 by using the formula (1). The belt of weak vertical wind shear at 10°N over ENP is found in both the experiment and JRA-55, thus confirming that the model experiment reproduces the actual field.

TCG over ENP is mostly located in the region of weak vertical wind shear (Fig. 4 and 7). TCG over WNP is also located in this region. These results confirm the well-known view that this belt of weak vertical wind shear creates TCG over the entire NP and indicates that the vertical wind shear has an important role in TCG over NP, as shown by Murakami et al. (2017).

Herein, we showed that CTL well reproduces the TCG of 2015. We found here the specific factors of the environmental field in 2015; that is, the westerly winds and vertical wind shear are important for TCG over WNP of 2015, while vertical wind shear is important for TCG over ENP of 2015. However, we did not understand what causes these environmental fields. The following section focuses on SST over the PMM region and the IO region and analyzes the relationship between SST and the environmental fields.

4. Effects of PPMM and the IO warming on TCG under the super El Niño condition

This section examines how the simultaneous effects of the IO warming and PPMM on TCG under the influence of the super El Niño that occurred in 2015. Table 1 shows the sensitivity experiments in which only the SST of the PMM region or the IO region was changed (i.e., PMMclm experiment and IOclm experiment). The sensitivity of each SST region is examined as compared to CTL.

Figure 8 shows the distribution of the TCG sites as the number of TCG points counted in boxes of 5° × 5°. Figure 8a shows the distribution in CTL and Figs. 8b and 8c show the difference in distribution between PMMclm and CTL (Pmmclm – CTL) and between IOclm and CTL (IOclm – CTL), respectively.

When comparing the PMMclm and CTL (PMMclm – CTL; Fig. 8b), the number of TCG over the WNP increases while the number of TCG over the ENP decreases. This result indicates that the warmer SST over the PMM region reduces the number of TCG over WNP and increases it over ENP. Our results on the relationship between TCG over ENP and SST over the PMM region are consistent with Murakami et al. (2017). However, the relationship between TCG over WNP and SST over the PMM region is the opposite of that found by Zhang et al. (2016), which shows that the positive PMM phase favors TCG over WNP. This inconsistency will be clarified below.

Figure 9a shows the SLP of the PMMclm experiment and the differences in the SLP between the sensitivity experiments and CTL (Fig. 3a). Diagonal line areas show where the t-test is 5 % significant. The SLP in the western part of WNP is lower in the PMMclm experiment than in CTL, while the SLP from the eastern part of WNP to ENP becomes higher than the SLP in CTL. This east-west contrast of the SLP anomaly is consistent with the difference in TCG shown in Fig. 8b. It implies that if SST over the PMM region is warmer, the environmental fields for TCG over the western part of WNP are more unfavorable. In contrast, the environmental fields from the eastern part of WNP to ENP are more favorable.

For the IOclm experiment (Fig. 8c), although the number of TCG over WNP increases, the number of TCG over ENP does not show a significant difference. This result indicates that the cooler SST over IO (IOclm - CTL) impacts increasing the number of TCG over WNP. In comparison, the cooler SST over the IO region does not radically change the number of TCG over ENP.

Figure 9b is similar to 9a, but for the results of the IO experiment. This sensitivity experiment shows that the SLP in the western part of WNP becomes lower than the SLP in CTL. However, in ENP, no such differences in the SLP exist. This result is consistent with the difference in TCG and indicates that the warmer IO affects the TCG only over WNP.

Figures 10a and 10b show zonal winds at 850hPa and positions of TC genesis for the PMMclm and IOclm experiments. Figures 10c and 10d show the difference in zonal winds for these two sensitivity experiments from CTL. Diagonal line areas show where the t-test is 5 % significant. Figure 10c shows that westerly winds become stronger in the equatorial WNP from the Philippines towards the dateline (Figs. 10a and 10b) compared to CTL (Fig. 3c). Figure 10d also shows a similar magnitude of the difference in westerly winds in the equatorial WNP, but it does not impact ENP.

We consider that the increase in the number of TCG over WNP (Fig. 8) is due to the intensification of westerly winds of the monsoon trough. In addition, Figs. 11a and 11b indicate that TC genesis mainly occurs in the region of the wind shear line between the westerly and the easterly winds over WNP. Therefore, warmer SST over the PMM region and IO weakens the westerly winds corresponding to the monsoon trough, and as a result, TCG over WNP decreases.

Figures 11a and 11b show the average vertical wind shear of the PMMclm and IOclm experiments, and Figs. 11c and 11d show the differences in vertical wind shear between the two sensitivity experiments and CTL. Diagonal line areas show where the t-test is 5 % significant. Figure 11c shows stronger shear over ENP in the PMMclm experiment. In contrast, Fig. 11d shows that the vertical shear over ENP does not have a notable change.

The decrease in the number of TCG over ENP (Fig. 8) is due to the intensification of vertical wind shear. This result indicates that warmer SST in the PMM region weakens the vertical wind shear over ENP and increases TCG, while warmer SST over the IO region has no impact on TCG over ENP.

Figures 11c and 11d also show that when the SST in the PMM region and the IO region is cooler, the vertical wind shear over WNP is stronger; this suggests that these sensitivity experiments are unfavorable for TCG over WNP.

However, as shown in Figs. 8b and 8c, the number of TCG in each sensitivity experiment is higher than that in CTL, which is inconsistent with the results shown by Figs. 11c and 11d. Therefore, we conclude that the influence of the SST in the PMM and the IO regions on TCG over WNP in 2015 can be attributed more to the westerly wind modulation represented by the monsoon trough than to the vertical wind shear modulation.

This section showed that when the SST in the PMM region and the IO region is warmer under strong 2015 El Niño, the westerly winds over WNP are weaker, reducing the number of TCG over WNP. When vertical wind shear over ENP is weaker, the number of TCG over ENP increases. Our results are similar to those reported in the previous studies (i.e., Zhan et al. 2011; Ha et al. 2015; Murakami et al. 2017) concerning the influence of the IO warming on TCG over WNP and the effect of the PPMM on TCG over ENP. However, our results differ from those shown in the previous studies regarding the influence of PPMM on TCG over WNP (Zhang et al. 2016; Zhan et al. 2017; Hong et al. 2018; Wu et al. 2018; Gao et al. 2018). These indicate that positive SSTAs in the PMM region cause a cyclonic response over WNP and that these anomalies provide favorable conditions for TCG over WNP. The relationship between the PPMM and the environmental fields of TCG over WNP will be discussed in the next section.

5. **The influence of the PPMM on the environmental fields on TCG over WNP in 2015**

To examine the relationship between the PPMM and the environmental fields of TCG, we conducted additional sensitivity experiments using the SSTAs shown in Figs. 1b and 1e-g. Figures 12a-c show the differences in the zonal wind field at 850hPa for the sensitivity experiments of PPMM for different reference conditions. Figure 12a shows the impact of PPMM on the condition of the SST in 2015 (Fig. 1a – 1c); Fig. 12b shows that the condition in which SST was warmer only in the El Niño region (Fig. 1e – 1f); Fig. 12c shows that for the climatological SST condition (Fig. 1g – 1b). In particular, the difference shown in Fig. 12c follows the previous study (Zhang et al. 2016).

Figure 12a shows an anomalous cyclonic circulation over ENP and an anomalous anticyclonic circulation over WNP. The latter causes the weakening of the monsoon trough (Fig. 10c). Figure 12b also shows anomalous circulation similar to Fig. 12a over WNP and ENP. Such anomalous circulation might be explained by the presence/absence of the PPMM under the super El Niño 2015 event and the co-existence of the PPMM and super El Niño, which lead to unfavorable environmental fields for TCG over WNP. Figure 12c shows the anomalous cyclonic circulation over WNP; this is similar to the results reported in Zhang et al. (2016) and indicates that the environmental fields of TCG are favorable under the PPMM. The result of the anomalous cyclonic circulation shown in Fig. 12c is the reverse of the results shown in Figs. 12a and 12b.

Our results indicate that the circulation response over WNP to the SSTA in the PMM region depends on El Niño-Southern Oscillation (ENSO) phase. The PPMM induces the anticyclonic response over WNP during El Niño events, while it induces the cyclonic response over WNP in the absence of El Niño. This result implies that the response to the SSTAs in the PMM and El Niño regions is not additive, which might explain the difference between our results and those from the previous studies; our research shows the role of the PPMM and El Niño on TCG over WNP while previous studies have focused on the relationship between TCG and the PPMM.

6. Summary and Conclusions

This study aimed to reveal the influence of the IO warming and the PPMM on TCG over NP during the super El Niño event in 2015. This study conducted perpetual July experiments for 30 months using NICAM. It was confirmed that CTL taking the climatological conditions of July 2015, successfully reproduced TCG and environmental fields, including the monsoon trough with zonal winds over the equatorial and sub-tropical NP.

We also investigated the impact of SSTAs in the PMM region and IO during the super El Niño event in 2015. For this purpose, we conducted the PMMclm and IOclm experiments and compared them with CTL. Both the PMMclm and IOclm experiments show lower SLP and stronger westerly winds over WNP than

CTL. This result indicates that SST warming in the two regions negatively affects TCG over WNP. In addition, the IOclm experiment shows that warming over IO is not responsible for anomalous vertical wind shear and has little influence on TCG over NP compared to CTL.

To examine the role of PPMM on TCG over WNP in 2015, we conducted additional experiments. We found that under the super El Niño condition, the difference in the presence (or absence) of the PPMM causes the environmental fields of TCG to become unfavorable (or favorable).

The present study confirmed variability in TCG caused by the internal atmospheric modes. The number of TCs shows a large variance under the same SST condition. Moreover, TC activities are not only dependent on the environmental conditions (such as SST distribution) but also are a function of variability related to fluctuations (such as intra-seasonal variability under the same environmental conditions). This effect should be considered to understand better the relationship between TC activities and SST patterns for improved seasonal forecasting.

The effects of atmosphere-ocean interactions were not considered in this study. It is known that the interactions between the atmosphere and the ocean affect TC activities. Moreover, the effect of TCs on the cooling of SST through oceanic upwelling is significant. For example, Schade and Emanuel (1999) studied the differences in TC development using atmospheric and coupled atmosphere-ocean models. They showed that based on the atmospheric model, the pressure of the typhoon was approximately 30 hPa higher when compared to the coupled atmosphere-ocean model. Moreover, Lin et al. (2008) showed that local subsurface ocean warming induces strong typhoons. To consider the interactions between the large-scale atmospheric circulation and the SST distribution at the seasonal scale, we will incorporate a high-resolution coupled atmosphere-ocean model in the future (e.g., Miyakawa et al. 2017) to analyze the relationship between atmosphere-ocean interaction and TCs.

Data Availability Statement

The numerical experimental data are provided by requests to the authors.

Acknowledgments

We used the Japanese 55-year Reanalysis (JRA-55) data in this study. We also used the Grads software to plot the results and Oakleaf-FX10 of the Information Technology Center of the University of Tokyo to conduct all numerical experiments. This work is supported by the FLAGSHIP2020, MEXT within the priority study (No.4: Advancement of meteorological and global environmental predictions utilizing observational "Big Data") and by MEXT (JPMXP1020200305) under the "Program for Promoting Researches on the Supercomputer Fugaku" (Large Ensemble Atmospheric and Environmental Prediction for Disaster Prevention and Mitigation).

References

Bluden, J., and D. S. Arndt, Eds., 2016: State of the Climate in 2015. Bull. Amer. Meteor. Soc., 97 (8), S1-S275, DOI:10.1175/2016BAMSStateoftheClimate.1

Camargo, S. J., 2013: Global and regional aspects of tropical cyclone activity in the CMIP5 models. J. Clim. 26, 9880–9902. doi:10.1175/JCLI-D-12-00549.1.

Camargo, S. J., and A. H. Sobel, 2005: Western North Pacific tropical cyclone intensity and ENSO. J. Climate, **18**, 2996–3006, doi:10.1175/ JCLI3457.1.

Camargo, S. J., M. C. Wheeler and A. H. Sobel, 2009: Diagnosis of the tropical cyclogenesis using an empirical index. JAS, 75, 3061-3074, doi:10.1175/2009JAS3101.1.

Cess, R. D., and J. B. Klemp, 1988: A methodology for understanding and intercomparing atmospheric climate feedback processes in general circulation models. J. Geophys. Res., **93**, 8305-8314. doi:10.1029/JD093iD07p08305.

Chan, J. C. L., 2000: Tropical cyclone Activity over the western north Pacific associated with El Niño and La Niña events. J. Climate, **13**, 2960-2972, doi:10.1175/1520-0442(2000)013<2960:TCAOTW>2.0.CO;2.

Chan. J. C. L., and K. S. Liu, 2004: Global warming and western north Pacific typhoon activity from an observational perspective. J. Climate, **17**, 4590-4602, doi:10.1175/3240.1.

Chavas, D. R., and K. A. Emanuel, 2010: A QuikSCAT climatology of tropical cyclone size. Geophys. Res. Lett, 37, L18816, doi:10.1029/2010GL044558.

Chen, T. C., S. Y. Wang, and M. C. Yen, 2006: Interannual variation of tropical cyclone activity over the western North Pacific. J. Climate, **19**, 5709–5720, doi:10.1175/JCLI3934.1.

Chiang, J. C. H., and D. J. Vimont, 2004: Analogous Pacific and Atlantic meridional modes of tropical atmosphere–ocean variability. J. Climate, **17**, 4143–4158, doi:10.1175/JCLI4953.1.

Chikira, M., Yamada, Y., Abe-Ouchi, A., Satoh, M., 2022: Response of convective systems to the orbital forcing of the last interglacial in a global nonhydrostatic atmospheric model with and without a convective parameterization. Clim. Dyn., https://doi.org/10.1007/s00382-021-06056-5

Emanuel, K. A., and D. S. Nolan, 2004: Tropical cyclone activity and global climate. Preprints, 26th Conf. on Hurricanes and Tropical Meteorology, Miami, FL, Amer. Meteor. Soc., 240–241.

Gao, S., L. Zhu, W. Zhang, and Z. Chen, 2018: Strong modulation of the Pacific meridional mode on the occurrence of intense tropical cyclones over the western north Pacific. J. Climate, **31**, 7739-7749, doi:10.1175/JCLI-D-17-0833.1.

Ha, Y., Z. Zhong, X. Yang and Y. Sun, 2015: Contribution of east Indian Ocean SSTA to western north Pacific tropical cyclone activity under El Niño/La Niña conditions. Int. J. Climatol, **35**, 506-519, doi: 10.1002/joc.3997

Hong, C. –C., and M. –Y. Lee, H. –H. Hsu, and W. –L. Tseng, 2018: Distinct influences of the ENSO-like and PMM-like SST anomalies on the mean TC genesis location in the western north Pacific: the 2015 summer as an extreme example. J. Climate., **31**, 3049-3059, doi:10.1175/JCLI-D-17-0504.1.

Iga, S., H. Tomita, Y. Tsushima, and M. Satoh, 2007: Climatology of a nonhydrostatic global model with explicit cloud processes. Geophys. Res. Lett., **34**, L22814, doi:10.1029/2007GL031048.

Knaff, J. A., C. R. Sampson, M. Demaria, T. P. Marchok, J. M. Gross, and C J. Mcadie, 2007: Statistical tropical cyclone wind radii prediction using climatology and persistence. Wea. Forcasting, **22**, 781-791, doi:10.1175/WAF1026.1.

Knapp, K. R., M. C. Kruk, D. H. Levinson, H. J. Diamond, and C. J. Neumann, 2010: The International Best Track Archive for Climate Stewardship (IBTrACS). Bull. Amer. Meteor. Soc., **91**, 363–376, doi:10.1175/2009BAMS2755.1.

Kobayashi, S., Y. Ota, Y. Harada, A. Ebita, M. Moriya, H. Onoda, K. Onogi, H. Kamahori, C. Kobayashi, H. Endo, K. Miyaoka, and K. Takahashi, 2015: The JRA-55 Reanalysis: General specifications and basic characteristics. J. Meteor. Soc. Japan, **93**, 5-48, doi:10.2151/jmsj.2015-001.

Kodama, C., Y. Yamada, A. T. Noda, K. Kikuchi, Y. Kajikawa, T. Nasuno, T. Tomita, T. Yamaura, T. G. Takahashi, M. Hara, Y. Kawatani, M. Satoh, and M. Sugi, 2015: A 20-year climatology of a NICAM AMIP-type simulation. J. Meteor. Soc. Japan, **93**, 393-424, doi:10.2151/jmsj.2015-024

Kodama, C., Ohno, T., Seiki, T., Yashiro, H., Noda, A. T., Nakano, M., Yamada, Y., Roh, W., Satoh, M., Nitta, T., Goto, D., Miura, H., Nasuno, T., Miyakawa, T., Chen, Y.-W., and Sugi, M., 2021: The Nonhydrostatic ICosahedral

Atmospheric Model for CMIP6 HighResMIP simulations (NICAM16-S): experimental design, model description, and impacts of model updates. Geosci. Model Dev., 14, 795–820. https://doi.org/10.5194/gmd-14-795-2021

Lander, M. A., 1994: An exploratory analysis of the relationship between tropical strom formation in the western north Pacific and ENSO, Mon. Wea. Rev., **122**, 636-651, doi:10.1175/1520-0493(1994)122<0636:AEAOTR>2.0.CO;2.

L'Heureux M. L., K. Takahashi, A. B. Watkins, A. G. Barnston, E. J. Becker, T. E. T. E. Di Liberto, F. Gamble, J. Gottschalck, M. S. Halpert, B. Huang, K. Mosquera-Vásquez, and A. T. Wittenberg, 2016: Observing and predicting the 2015-16 El Niño. Bull Amer. Meteor. Soc., **98**, 1363-1382, doi:10.1175/BAMS-D-16-0009.1.

Lin, I. I., C. C. Wu and I. F. Pun, 2008: Upper-ocean thermal structure and the western North Pacific category 5 typhoons. Part I: ocean Features and the category 5 typhoons' Intensification. Mon. Wea. Rev., **136**, 3288-3306, doi:10.1175/2008MWR2277.1.

Oouchi, K., J. Yoshimura, H. Yoshimura, R. Mizuta, S. Kusunoki, and A. Noda, 2006: Tropical cyclone climatology in a global warming climate as simulated in a 20 km mesh global atmospheric model: Frequency and intensity analysis. J. Meteor. Soc. Japan, **84**, 259-276, doi:10.2151/jmsj.84.259

Miura, H., M. Satoh, T. Nasuno, A. T. Noda and K. Oouchi, 2007: A Madden-Julian Oscillation event simulated using a global cloud-resolving model. Science, **318**, 1763-1765. doi:10.1126/science.1148443

Miyakawa, T., M. Satoh, H. Miura, H., Yashiro, A. T. Noda, Y. Yamada, C. Kodama, M. Kimoto and K. Yoneyama, 2014: Madden-Julian Oscillation prediction skill of a new-generation global model. Nature Commun., **5**, 3769. doi:10.1038/ncomms4769.

Miyakawa, T., H. Yashiro, T. Suzuki, H. Tatebe and M. Satoh, 2017: A Madden-Julian Oscillation event remotely accelerates ocean upwelling to abruptly terminate the 1997/1998 super El Niño. Geophys. Res. Lett., DOI:10.1002/2017GL074683

Murakami, H., G. A. Vecchi, T. L. Delworth, A. T. Wittenberg, S. Underwood, R. Gudgel, X. Yang, L. Jia, F. Zeng, K. Paffendorf and W. Zhang, 2017: Dominat role of subtropical Pacific warming in extreme eastern Pacific seasons: 2015 and future. J. Climate, **30**, 243-264, doi:10.1175/JCLI-D-16-0424.1.

Nakanishi, M. and H. Niino, 2004: An improved Mellor-Yamada Level-3 model with condensation physics: It's design and verification. Bound.-Layer Meteor., **112**, 1-31. doi:10.1023/B:BOUN.0000020164.04146.98.

Nakano, M., M. Sawada, T. Nasuno, and M. Satoh, 2015: Intraseasonal variability and tropical cyclogenesis in the western North Pacific simulated by a global nonhydrostatic atmospheric model. Geophys. Res. Lett., **42**, 565-571, doi:10.1002/2014GL062479.

Ritchie, E. A., and G. J. Holland, 1999: Large-scale patterns associated with tropical cyclogenesis in the western Pacific. Mon. Wea. Rev., **127**, 2027-2043, doi:10.1175/1520-0493(1999)127<2027:LSPAWT>2.0.CO;2

Roberts, M. J., Camp, J., Seddon, J., Vidale, P. L., Hodges, K., Vanniere, B., et al., 2020 : Impact of model resolution on tropical cyclone simulation using the

HighResMIP–PRIMAVERA multimodel ensemble. J. Clim. 33, 2557–2583. doi:10.1175/JCLI-D-19-0639.1.

Satoh, M., T. Matsuno, H. Tomita, H. Miura, T. Nasuno, and S. Iga, 2008: Nonhydrostatic icosahedral atmospheric model (NICAM) for global cloud resolving simulations. J. Comput. Phys., **227**, 3486–3514, doi: 10.1016/j.jcp.2007.02.006

Satoh, M., H. Tomita, H. Yashiro, H. Miura, C. Kodama, T. Seiki, A. T. Noda, Y. Yamada, D. Goto, M. Sawada, T. Miyoshi, Y. Niwa, M. Hara, T. Ohno, S. Iga, T. Arakawa, T. Inoue and H. Kubokawa, 2014: The non-hydrostatic icosahedral atmospheric model: description and development. Prog. in Earth and Planet. Sci. **1**: 18, doi: 10.1186/s40645-014-0018-1.

Satoh, M., Y. Yamada, M. Sugi, C. Kodama and A. T. Noda, 2015: Constraint on future change in global frequency of tropical cyclones due to global warming. J. Meteorol. Soc. Japan, **93**, 489-500, doi:10.2151/jmsj.2015-025.

Satoh, M., H. Tomita, H. Yashiro, Y. Kajikawa, Y. Miyamoto, T. Yamaura, T. Miyakawa, M. Nakano, C. Kodama, A. T. Noda, T. Nasuno, Y. Yamada and Y.

Fukutomi, 2017: Outcomes and challenges of global high-resolution non-hydrostatic atmospheric simulations using the K computer. Progress in Earth and Planetary Science, 4, 13, doi:10.1186/s40645-017-0127-8.

Schade, L. R., and K. A. Emanuel, 1999: The ocean's effect on the intensity of tropical cyclones: results from a simple coupled atmosphere-ocean model. J. Atmos. Sci., **56**, 642-651, doi: 10.1175/1520-0469(1999)056<0642:TOSEOT>2.0.CO;2.

Sekiguchi, M. and T. Nakajima, 2008: A k-distribution-based radiation code and its computational optimization for an atmospheric general circulation model. J. Quant. Spectrosc. Radiat. Transfer., **109**, 2779-2793, doi:10.1016/j.jqsrt.2008.07.013

Takasuka, D., T. Miyakawa, M. Satoh, H. Miura, 2015: Topographical effects on the internally produced MJO-like disturbances in an aqua-planet version of NICAM. SOLA, **11**, 170-176, doi:10.2151/sola.2015-038

Takasuka, D., M. Satoh, T. Miyakawa and H. Miura, 2018: Initiation Processes of the Tropical Intraseasonal Variability Simulated in an Aqua-planet Experiment:

What is the Intrinsic Mechanism for MJO Onset? J. Adv. Model. Earth Syst., accepted.

Takata, K., S. Emori, and T. Watanabe, 2003: Development of the minimal advanced treatments of surface interaction and runoff. Global. Planet. Change, **38**, 209–222, doi: 10.1016/S0921-8181(03)00030-4

Timmermann, A., S. –I. An, J. –S. Kug, F. –F. Jin, W. Cai, A. Capotondi, K. Cobb. M. Lengaigne, M. J. McPhaden, M. F. Stuecker, K. Stein, A. T. Wittenberg, K. –S. Yun, T. Bayr, H. –C. Chen, Y. Chikamoto, B. Dewitte, Di. Dommenget, P. Grothe, E. Guilyardi, Y. –G. Ham, M. Hayashi, S. Ineson, D. Kang, S. Kim, W. Kim, A. Santoso, K. Takahashi, A. Todd, G. Wang, G. Wang, R. Xie, W. –H. Yang, S. –W. Yeh, J. Yoon, E. Zeller, and X. Zhang, 2018: El Niño-Southern oscillation complexity. Nature, **559**, 535-545, doi:10.1038/s41586-018-0252-6.

Tomita, H., and M. Satoh, 2004: A new dynamical framework of nonhydrostatic global model using the icosahedral grid. Fluid Dyn. Res., **34**, 357–400, doi:10.1016/j.fluiddyn.2004.03.003

Tomita, H., 2008: New microphysical schemes with five and six categories by diagnostic generation of cloud ice. J. Meteor. Soc. Japan, **86A**, 121–142, doi: 10.2151/jmsj.86A.121

Walsh, K., M. Fiorino, C. W. Landsea, and K. L. McInnes, 2007: Obsjectively determined resolution-dependent threshold criteria for the detection of tropical cyclones in climate models and reanalyses. J. Climate, **20**, 2307-2314, doi:10.1175/JCLI4074.1.

Wang, B., and J. C. L. Chan, 2002: How strong ENSO events affect tropical storm activity over the western North Pacific. J. Climate, **15**, 1643–1658, doi:10.1175/1520-0442(2002)015,1643: HSEEAT.2.0.CO;2.

Wu, L., Z. Wen, R. Huang, and R. Wu, 2012: Possible linkage between the monsoon trough variability and the tropical cyclone activity over the western North Pacific. Mon. Wea. Rev., **140**, 140–150, doi:10.1175/MWR-D-11-00078.1.

Wu, Y. K., C. –C. Hong, and C. –T. Chen, 2018: Distict effects of the two strong El Niño events in 2015-2016 and 1997-1998 on the western north Pacific monsoon and tropical cyclone activity: role of subtropical eastern north Pacific warm SSTA. J. Geophys. Res., **123**, doi:10.1002/2018JC013798.

Xie, S.-P., K. Hu, J. Hafner, H. Tokinaga, Y. Du, G. Huang, and T. Sampe, 2009: Indian Ocean capacitor effect on Indo– western Pacific climate during the summer following El Niño. J. Climate, **22**, 730–747, doi:10.1175/2008JCLI2544.1.

Yamada, Y., M. Satoh, M. Sugi, C. Kodama, A. T. Noda, M. Nakano and T. Nasuno, 2017: Response of tropical cyclone activity and structure to global warming in a high-resolution global nonhydrostatic model. J. Clim., **30**, 9703-9724, doi:10.1175/JCLI-D-17-0068.1.

Yamada, Y., C. Kodama, M. Satoh, M. Nakano, T. Nasuno, and M. Sugi, 2019: High-resolution ensemble simulations of intense tropical cyclones and their internal variability during the El Ninos of 1997 and 2015. Geophys. Res. Lett., **46**, 7592-7601, doi:10.1029/2019GL082086.

Yamada, Y., Kodama, C., Satoh, M., Sugi, M., Roberts, M. J., Mizuta, R., Noda, A. T., Nasuno, T., Nakano, M., Vidale, P. L., 2021: Evaluation of the contribution of tropical cyclone seeds to changes in tropical cyclone frequency due to global warming in high-resolution multi-model ensemble simulations. Progress in Earth and Planetary Science, 8, 11. https://doi.org/10.1186/s40645-020-00397-1

Yoshida, R., and H. Ishikawa, 2013: Environmental factors contributing to tropical cyclone genesis over the western north Pacific. Mon. Wea. Rev., **141**, 451-467, doi:10.1175/MWR-D-11-00309.1.

Yoshizaki, M., S. Iga and M. Satoh, 2012: Eastward-propagating property of large-scale precipitation systems simulated in the coarse-resolution NICAM and an explanation of its formation. SOLA, **8**, 21-24. doi:10.2151/sola.2012-006

Zhan, R., Y. Wang, and C. C. Wu, 2011: Impact of SSTA in the East Indian Ocean on the frequency of northwest Pacific tropical cyclones: A regional atmospheric model. J. Climate, **24**, 6227–6242, doi:10.1175/JCLI-D-10-05014.1.

Zhan, R., Y. Wang and Q. Liu, 2017: Salient differences in tropical cyclone activity over the western North Pacific between 1998 and 2016. J. Climate, **30**, 9979-9997, doi:10.1175/JCLI-D-17-0263.1.

Zhang, W., G. A. Vecchi, H. Murakami, G. Villarini, and L. Jia, 2016: The Pacific meridional mode and the occurrence of tropical cyclones in the western North Pacific. J. Climate, **29**, 381–398, doi:10.1175/JCLI-D-15-0282.1.

List of Figure captions

Fig. 1 SST [K] distributions of (a) the 2015 experiment, (b) the Allclm experiment, (c) the PMMclm experiment, (d) the INDclm experiment, (e) the PMM/El Niño2015 experiment, (f) the El Niño2015 experiment and (g) the PMM2015 experiment. Only SSTs in the region [30°E–85°W, 60°S–60°N] are shown. The contours denote the values of SST in July 2015, and the shades are the differences between experiments and the climate value (1982–2011, July average). Bold lines show that SST is 300 K. Solid lines of the low latitude side are drawn every 1 K, while solid lines of the high latitude side are drawn every 3 K.

Fig. 2 Time series (moving average of anteroposterior two weeks) of the domain mean surface temperature for 46 months in CTL (the experiment under the July 2015 condition). The black line denotes temperature over the Eurasian continent [60–120°E, 50–60°N], and the blue line denotes temperature over the Indochinese Peninsula [98–106°E, 14–24°N].

Fig. 3 Average SLPs [hPa] over the 30 months of (a) CTL. (b) Same as (a) but for the SLP [hPa] of JRA-55 for JAS 2015. The contours in Figs. 3a and 3b denote SLP [hPa]. The shade denotes the difference between the simulation or JRA-55 and the climatology. Average zonal wind [$m\ s^{-1}$] at 850 hPa for the 30 months for (c) CTL. (d) Same as (c), but for the zonal wind of the JRA-55 data; JAS. Bold contours in (a) and (b) show that SLP is 1020 K. Thin Solid courves are drawn every 5 hPa.

Fig. 4 Distribution of TC genesis in CTL. Black triangles denote the positions of TCG per the experiment, and red triangles denote the observed TCG points analyzed by the IBTrACS in July 2015.

Fig. 5 Box and whisker plots of the number of TCs. From left to right; NP, WNP, and ENP in CTL. The orange circles are the average values, and the red circles are the observed number of TCG points in July 2015.

Fig. 6 Time–longitude diagram of the average zonal winds [m s^{-1}] (average from 0°N to 5°N) at 850 hPa over the 30 months of CTL. The black triangles are the positions of TC genesis from 5°N to 15°N in the experiment.

Fig. 7 Average vertical wind shear [m s^{-1}] for the 30 months for (a) CTL. (b) Same as (a), but for 2015JAS of JRA-55.

Fig. 8 Distribution of the number of TC genesis in (a) CTL. (b) Difference between the PMMclm and CTL experiments: PMMclm – CTL. (c) Difference between the IOclm and CTL experiments: IOclm – CTL. The number of TC-genesis is counted in boxes of 5 degrees square.

Fig. 9 (a) Average SLP [hPa] for the 30 months for the PMMclm experiment and difference between the PMMclm and CTL experiments: PMMclm – CTL. (b)

Same as (a), but for the IOclm experiment. The areas with diagonal lines show where the t-test is 5 % significant.

Fig. 10 Average zonal winds [m s^{-1}] at 850 hPa for the 30 months for (a) the PMMclm experiment and (b) the IOclm experiment. (c) Difference between the PMMclm and CTL experiments: PMMclm – CTL. (d) Difference between the IOclm and CTL experiments: IOclm – CTL. The black triangles are the positions of TC genesis in Fig. 10a and 10b. The areas withn diagonal lines show where the t-test is 5 % significant.

Fig. 11 Average vertical wind shear [m s^{-1}] for the 30 months for the (a) PMMclm experiment and (b) IOclm experiment. (c) Difference between the PMMclm and CTL experiments: PMMclm – CTL. (d) Difference between the IOclm and CTL experiments: IOclm – CTL. The areas with diagonal lines show where the t-test is 5 % significant.

Fig. 12 Differences of the wind vector (vector) [m s^{-1}] at 850 hPa and SST anomaly (shade) [K] (a) between the CTL and PMMclm experiments (CTL – PMMclm), (b) between the PMM/El Niño2015 and El Niño2015 experiments (PMM/El Niño2015 – Elño2015) and (c) between the PMM2015 and Allclm experiments (PMM2015 – Allclm). The contour shows (a) SST [K] in the PMMclm experiment, (b) SST in the El Niño2015 experiment and (c) SST [K] in the Allclm experiment.

List of Tables

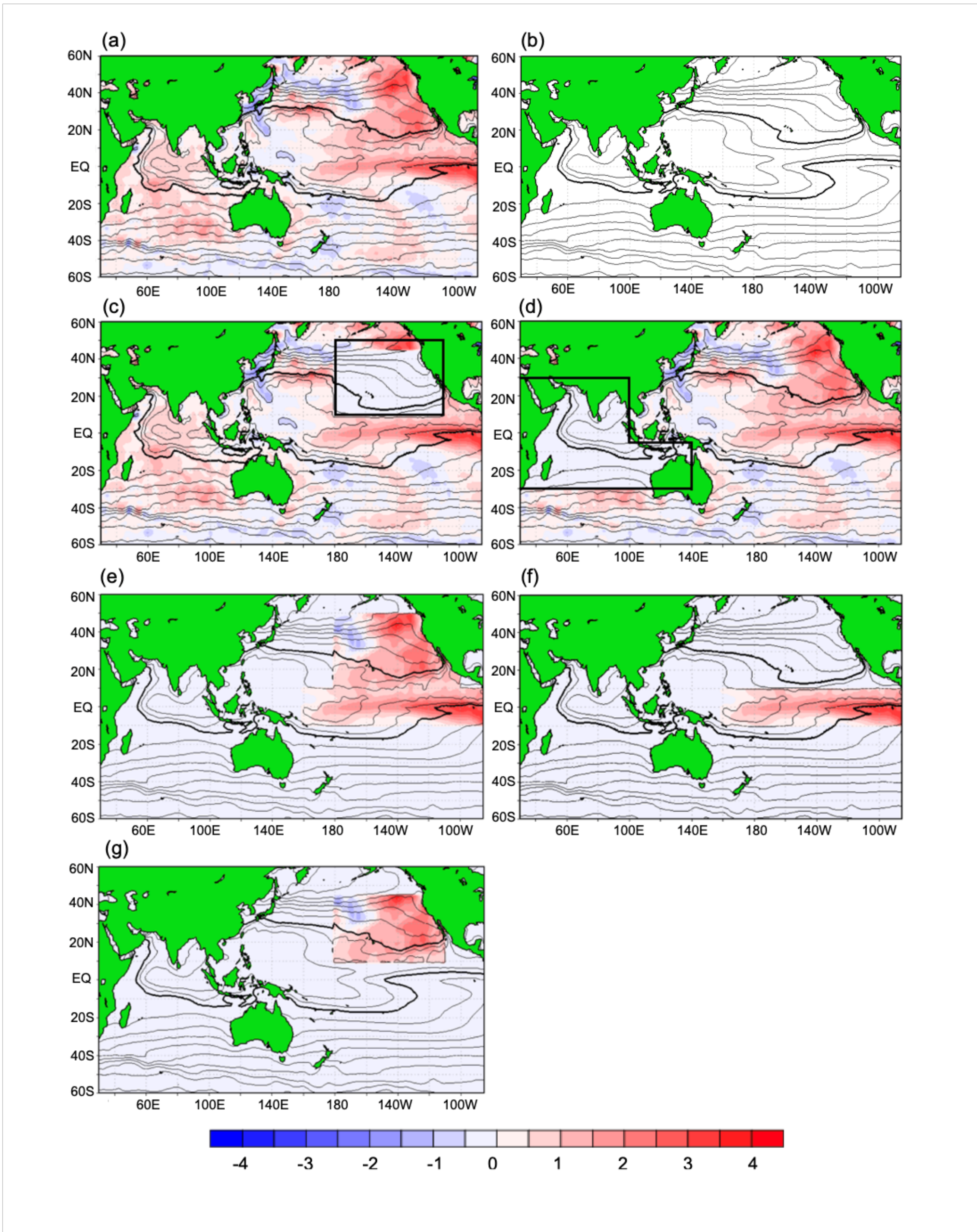

Fig. 1 SST [K] distributions of (a) the 2015 experiment, (b) the Allclm experiment, (c) the PMMclm experiment, (d) the INDclm experiment, (e) the PMM/El Niño2015 experiment, (f) the El Niño2015 experiment and (g) the PMM2015

experiment. Only SSTs in the region [30°E–85°W, 60°S–60°N] are shown. The contours denote the values of SST in July 2015, and the shades are the differences between experiments and the climate value (1982–2011, July average). Bold lines show that SST is 300 K. Solid lines of the low latitude side are drawn every 1 K, while solid lines of the high latitude side are drawn every 3 K.

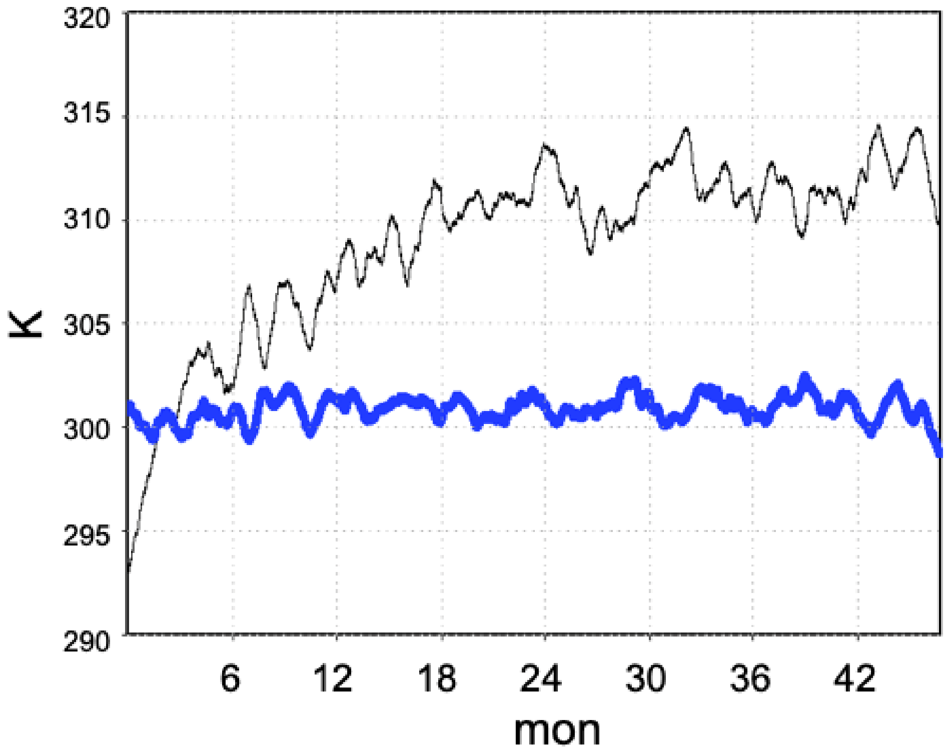

Fig. 2 Time series (moving average of anteroposterior two weeks) of the domain mean surface temperature for 46 months in CTL (the experiment under the July 2015 condition). The black line denotes temperature over the Eurasian continent [60–120°E, 50–60°N], and the blue line denotes temperature over the Indochinese Peninsula [98–106°E, 14–24°N].

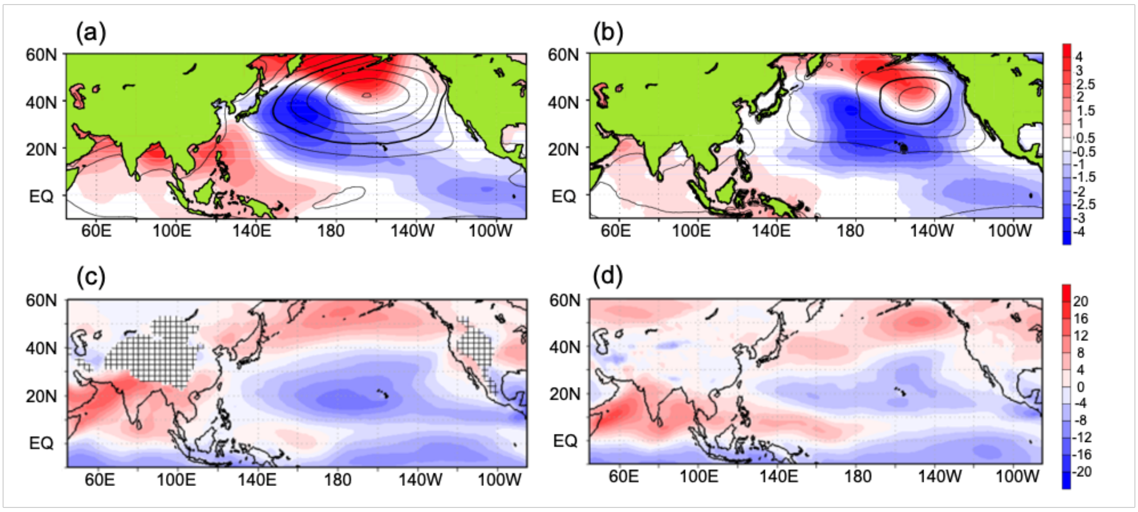

Fig. 3 Average SLPs [hPa] over the 30 months of (a) CTL. (b) Same as (a) but for the SLP [hPa] of JRA-55 for JAS 2015. The contours in Figs. 3a and 3b denote SLP [hPa]. The shade denotes the difference between the simulation or JRA-55 and the climatology. Average zonal wind [m s^{-1}] at 850 hPa for the 30 months for (c) CTL. (d) Same as (c), but for the zonal wind of the JRA-55 data; JAS. Bold contours in (a) and (b) show that SLP is 1020 K. Thin Solid courves are drawn every 5 hPa.

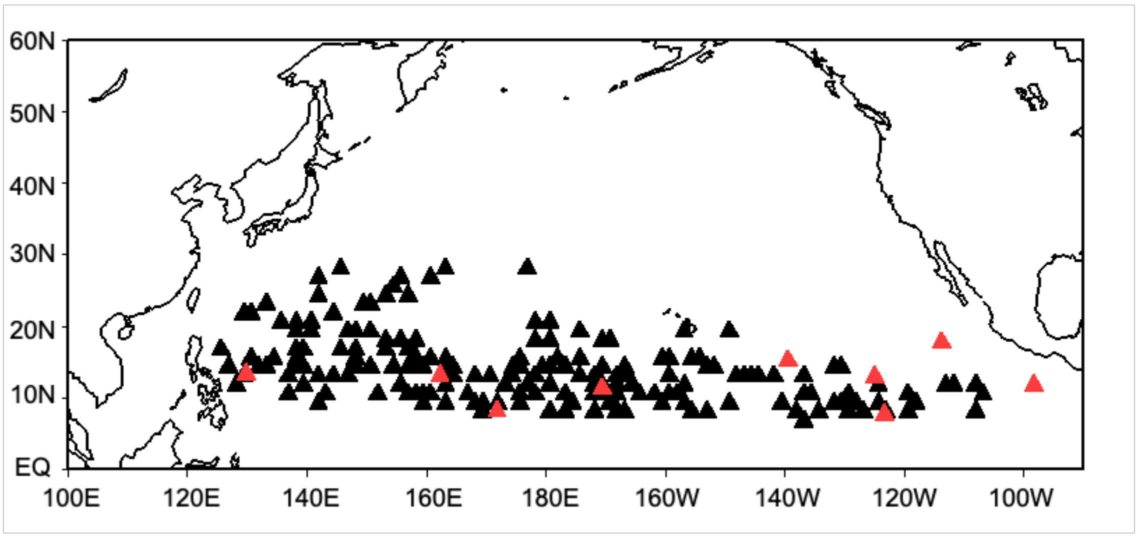

Fig. 4 Distribution of TC genesis in CTL. Black triangles denote the positions of TCG per the experiment, and red triangles denote the observed TCG points analyzed by the IBTrACS in July 2015.

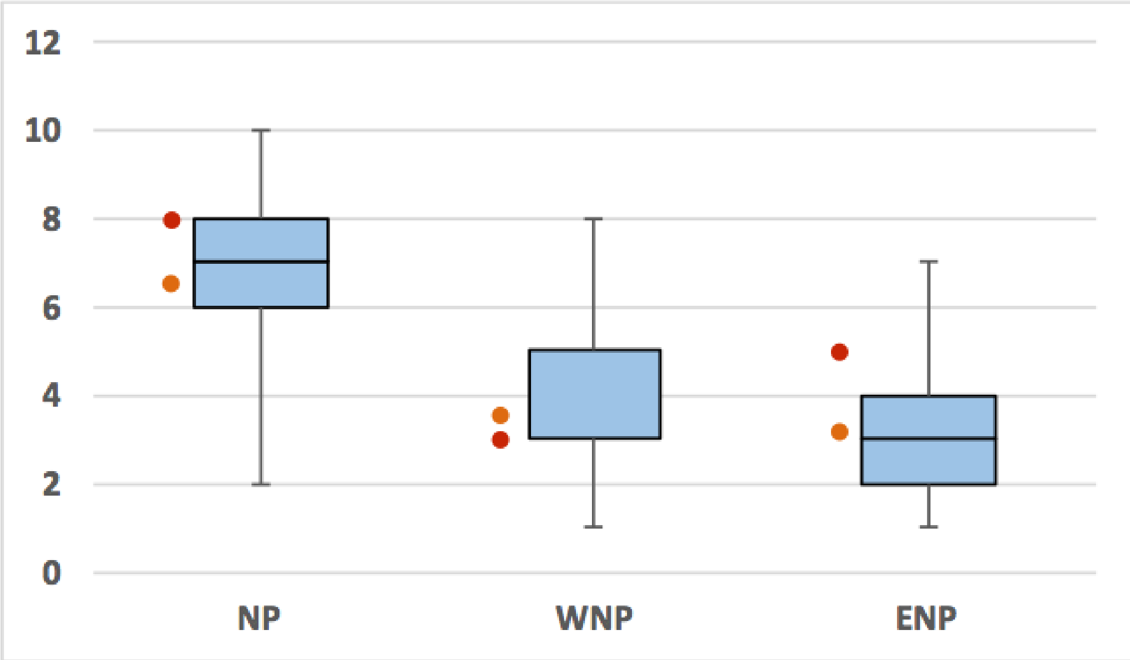

Fig. 5 Box and whisker plots of the number of TCs. From left to right; NP, WNP, and ENP in CTL. The orange circles are the average values, and the red circles are the observed number of TCG points in July 2015.

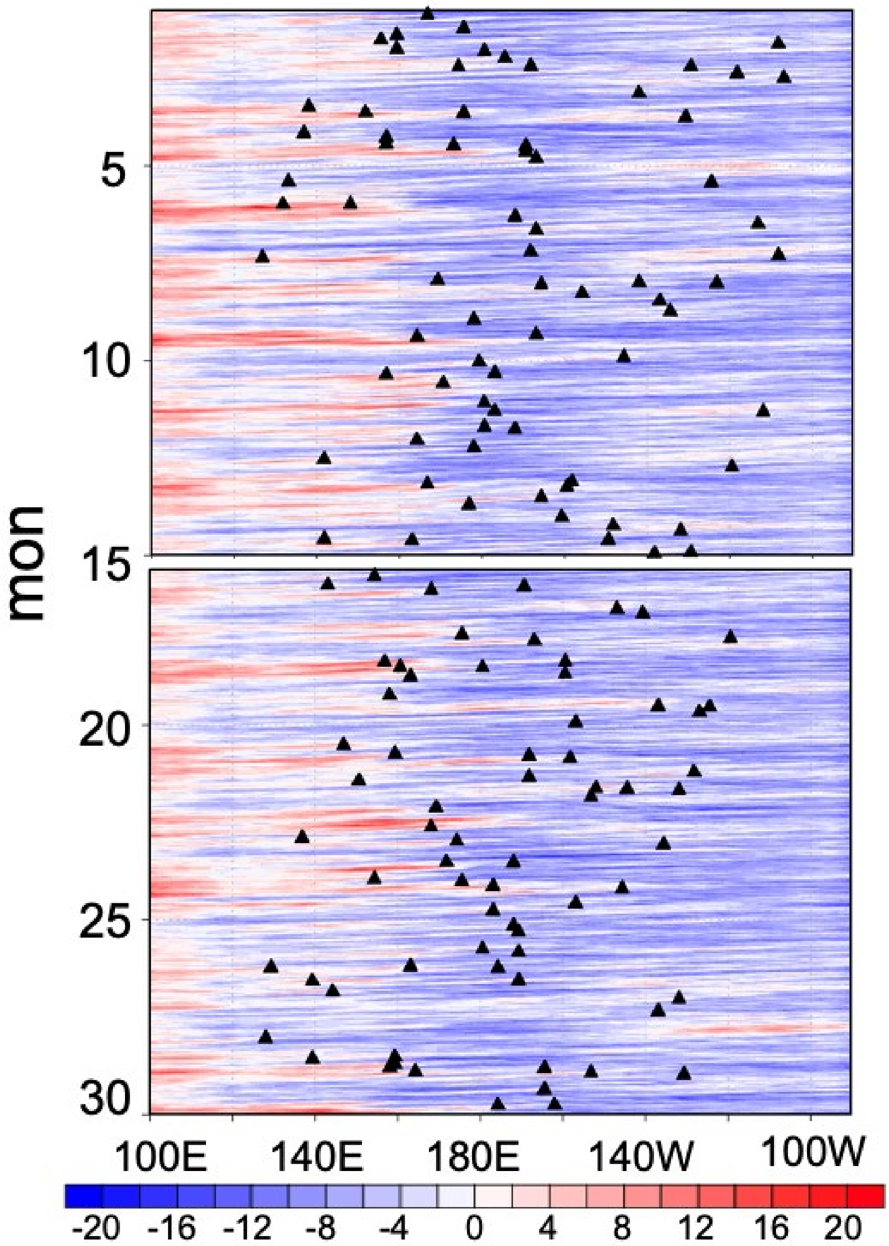

Fig. 6 Time–longitude diagram of the average zonal winds [m s^{-1}] (average from 0°N to 5°N) at 850 hPa over the 30 months of CTL. The black triangles are the positions of TC genesis from 5°N to 15°N in the experiment.

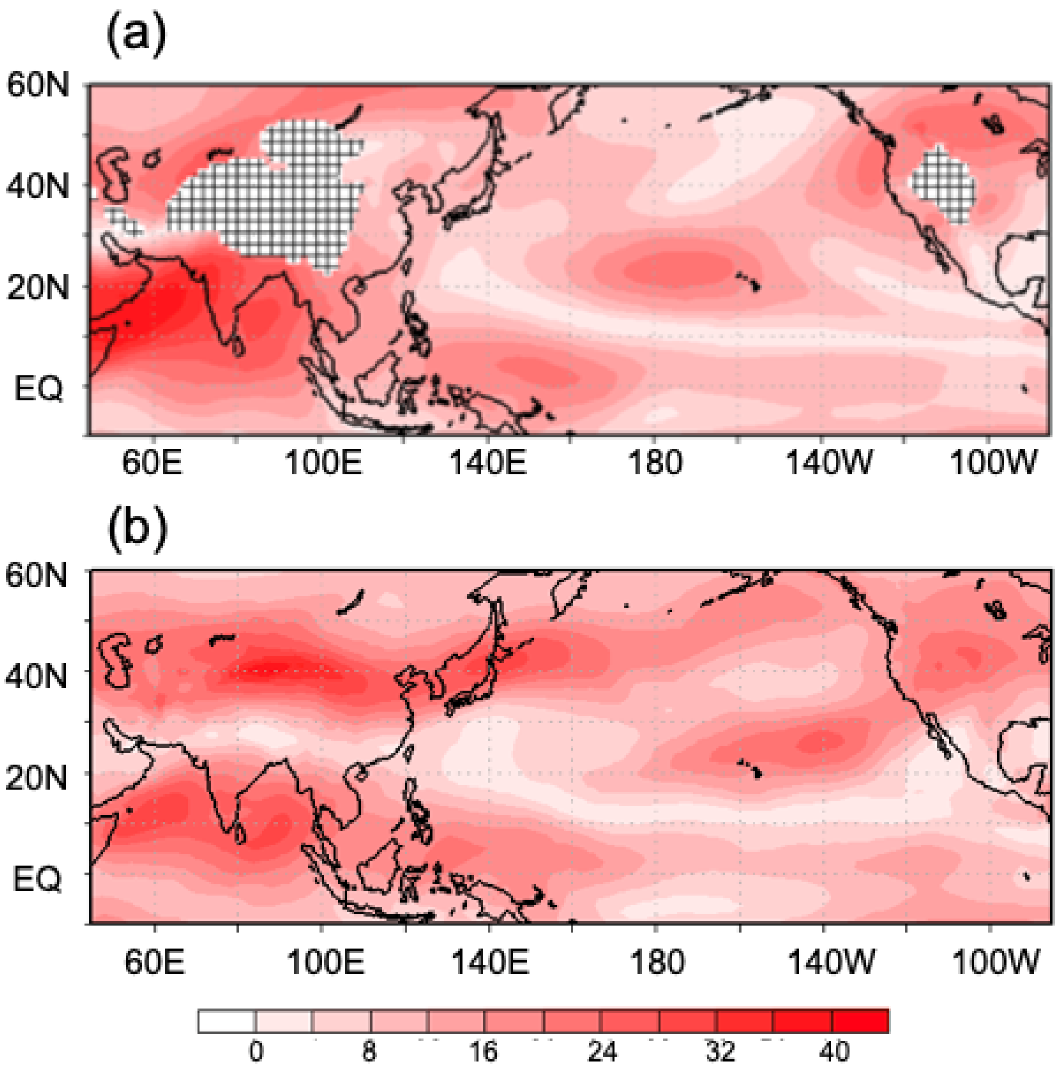

Fig. 7 Average vertical wind shear [m s^{-1}] for the 30 months for (a) CTL. (b) Same as (a), but for 2015JAS of JRA-55.

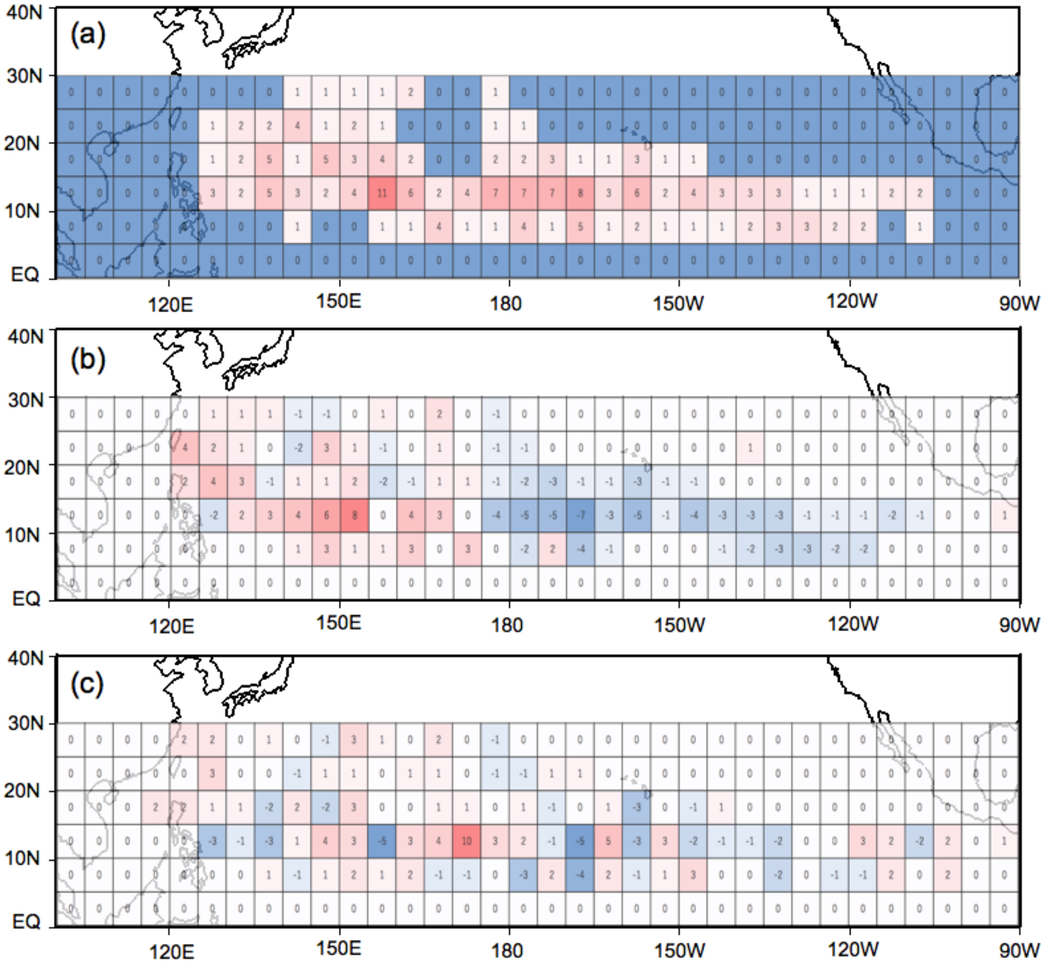

Fig. 8 Distribution of the number of TC genesis in (a) CTL. (b) Difference between the PMMclm and CTL experiments: PMMclm – CTL. (c) Difference between the IOclm and CTL experiments: IOclm – CTL. The number of TC-genesis is counted in boxes of 5 degrees square.

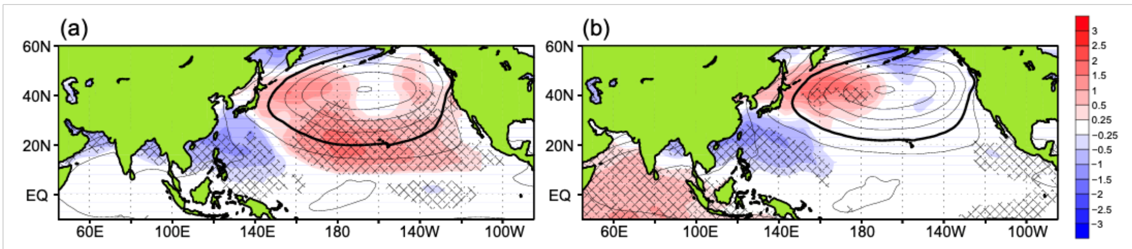

Fig. 9 (a) Average SLP [hPa] for the 30 months for the PMMclm experiment and difference between the PMMclm and CTL experiments: PMMclm – CTL. (b) Same as (a), but for the IOclm experiment. The areas with diagonal lines show where the t-test is 5 % significant.

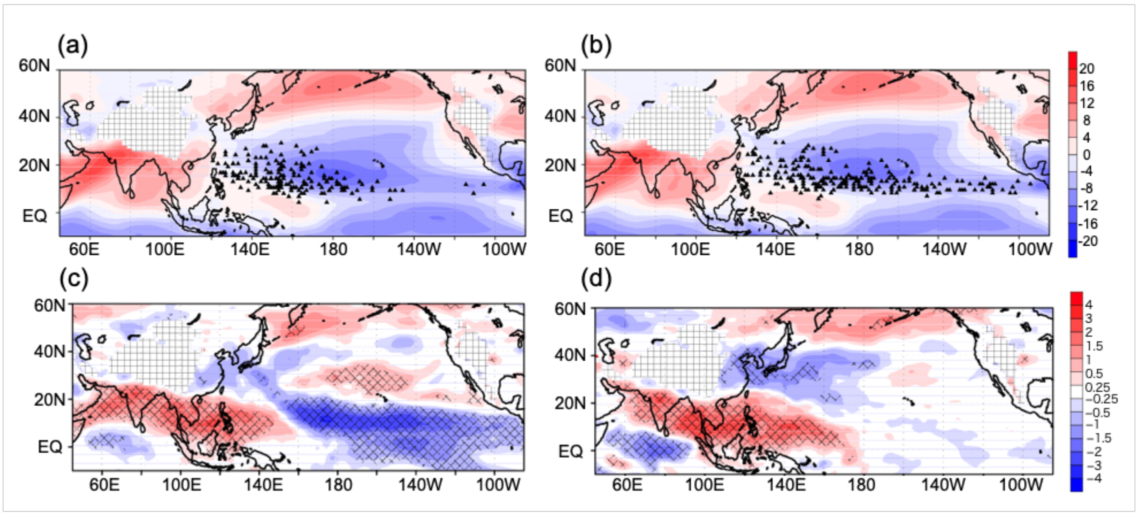

Fig. 10 Average zonal winds [m s^{-1}] at 850 hPa for the 30 months for (a) the PMMclm experiment and (b) the IOclm experiment. (c) Difference between the PMMclm and CTL experiments: PMMclm – CTL. (d) Difference between the IOclm and CTL experiments: IOclm – CTL. The black triangles are the positions of TC genesis in Fig. 10a and 10b. The areas withn diagonal lines show where the t-test is 5 % significant.

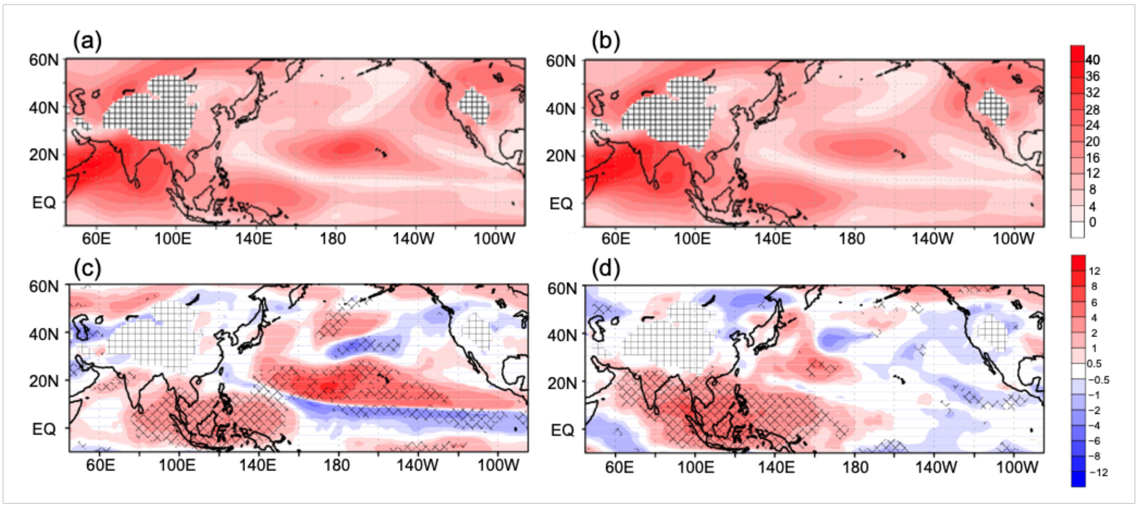

Fig. 11 Average vertical wind shear [m s^{-1}] for the 30 months for the (a) PMMclm experiment and (b) IOclm experiment. (c) Difference between the PMMclm and CTL experiments: PMMclm – CTL. (d) Difference between the IOclm and CTL experiments: IOclm – CTL. The areas with diagonal lines show where the t-test is 5 % significant.

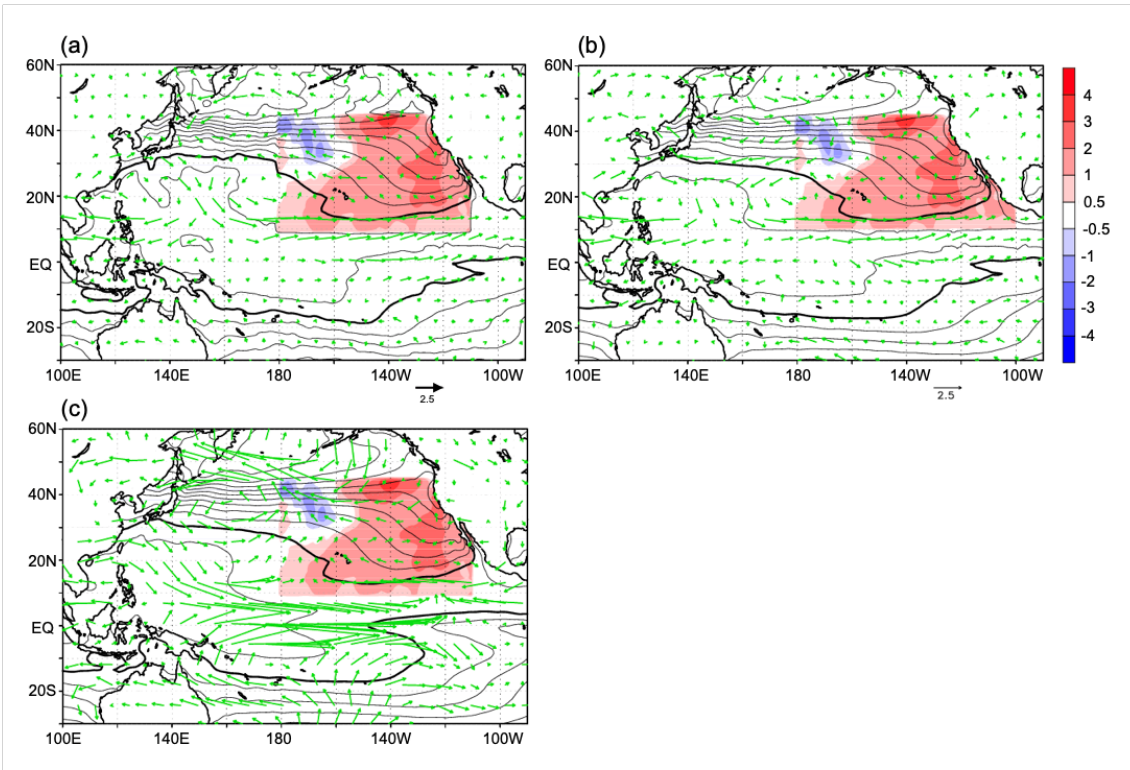

Fig. 12 Differences of the wind vector (vector) [m s^{-1}] at 850 hPa and SST anomaly (shade) [K] (a) between the CTL and PMMclm experiments (CTL – PMMclm), (b) between the PMM/El Niño2015 and El Niño2015 experiments (PMM/El Niño2015 – Elño2015) and (c) between the PMM2015 and Allclm experiments (PMM2015 – Allclm). The contour shows (a) SST [K] in the PMMclm experiment, (b) SST in the El Niño2015 experiment and (c) SST [K] in the Allclm experiment.

Table1: It is a table that arranges whether each experiment is used in the value of 2015 or the climate value in each SST region. Circles mean using SST of 2015 and cross mark mean using SST of climate value.

	El Niño region	PMM region	IO region	Other region
2015	◯	◯	◯	◯
Allclm	×	×	×	×
PMMclm	◯	×	◯	◯
INDclm	◯	◯	×	◯
El Niño + PMM real	◯	◯	×	×
El Niño real	◯	×	×	×
PMM real	×	◯	×	×